

Key Points:

- Angular response functions of SEM-2 MEPED electron and proton channels are derived by Geant4 simulation
- Combined with a dynamical radiation belt model, they show that the 0° telescope usually detects trapped rather than precipitating electrons
- Model fits to sample data are used to derive precipitating electron flux at $L = 4$ as a function of energy and longitude

Supporting Information:

- Supporting Information S1
- Data Set S1
- Data Set S2
- Data Set S3
- Data Set S4

Correspondence to:

R. S. Selesnick,
richard.selesnick@us.af.mil

Citation:

Selesnick, R. S., Tu, W., Yando, K. B., Millan, R. M., & Redmon, R. J. (2020). POES/MEPED angular response functions and the precipitating radiation belt electron flux. *Journal of Geophysical Research: Space Physics*, 125, e2020JA028240. <https://doi.org/10.1029/2020JA028240>




Received 15 MAY 2020

Accepted 31 JUL 2020

Accepted article online 20 AUG 2020

©2020. American Geophysical Union. This article has been contributed to by U.S. Government employees and their work is in the public domain in the USA.

POES/MEPED Angular Response Functions and the Precipitating Radiation Belt Electron Flux

R. S. Selesnick¹ , Weichao Tu² , K. Yando³, R. M. Millan⁴ , and R. J. Redmon⁵ 

¹Space Vehicles Directorate, Air Force Research Laboratory, Kirtland AFB, NM, USA, ²Department of Physics and Astronomy, West Virginia University, Morgantown, WV, USA, ³Jericho, VT, USA, ⁴Department of Physics and Astronomy, Dartmouth College, Hanover, NH, USA, ⁵National Centers for Environmental Information, National Oceanic and Atmospheric Administration, Boulder, CO, USA

Abstract Angular response functions are derived for four electron channels and six proton channels of the SEM-2 MEPED particle telescopes on the POES and MetOp satellites from Geant4 simulations previously used to derive the energy response. They are combined with model electron distributions in energy and pitch angle to show that the vertical 0° telescope, intended to measure precipitating electrons, instead usually measures trapped or quasi-trapped electrons, except during times of enhanced pitch angle diffusion. A simplified dynamical model of the radiation belt electron distribution near the loss cone, as a function of longitude, energy, and pitch angle, that accounts for pitch angle diffusion, azimuthal drift, and atmospheric backscatter is fit to sample MEPED electron data at $L = 4$ during times of differing diffusion rates. It is then used to compute precipitating electron flux, as function of energy and longitude, that is lower than would be estimated by assuming that the 0° telescope always measures precipitating electrons.

1. Introduction

Accurate measurement of energetic electron precipitation is of value in assessing both radiation belt loss and its effects on atmospheric chemistry. A valuable resource in this regard is the extensive data set collected by the Medium Energy Proton and Electron Detector (MEPED), in the Space Environmental Monitor subsystem, Version 2 (SEM-2) on the Polar Operational Environmental Satellite series (POES), operated by the National Oceanic and Atmospheric Administration (NOAA), and on the European MetOp satellites. Several operating satellites orbiting in different local-time planes provide global coverage, while MEPED telescopes on each satellite are paired in vertical and horizontal orientations to simultaneously measure trapped and precipitating particles.

Measured flux ratios from the horizontal (90°) and vertical (0°) telescopes have been used to infer efficiency of loss-cone filling by trapped electron scattering in several studies of radiation belt and atmospheric dynamics (Li et al., 2013; Ni et al., 2014; Nesse Tyssøy et al., 2016; Soria-Santacruz et al., 2015); others have used data from either telescope orientation alone (Peck et al., 2015; Pham et al., 2017; Pettit et al., 2019; Rodger et al., 2010). Typically, they have relied on nominal detector response characteristics as specified by the electronic and geometrical configurations of the MEPED instrumentation, which provide an energy threshold and angular field of view (FOV) for each of several available data channels, or have combined more accurate energy response functions (Yando et al., 2011) with a nominal FOV angular response. The purpose of this work is to determine more accurate angular response functions to be used in combination with the energy response, describe how application of the full instrumental response modifies inferred precipitating electron flux, and derive sample results for precipitating flux based on fits of a dynamical radiation belt model to measurements taken over a range of magnetospheric conditions.

2. MEPED Response Functions

The MEPED electron and proton telescopes are described in detail by Evans and Greer (2000). The electron telescope contains a single silicon detector and three channels, labeled E1, E2, and E3, are defined by deposited energy threshold levels. They typically respond to electrons with incident kinetic energy $E > 30$, 100, and 300 keV, respectively. The proton telescope contains two silicon detectors, and six channels are

defined by combinations of the two energy deposits at various threshold levels. Incident proton energy ranges for these channels are (P1) 30–80 keV, (P2) 80–240 keV, (P3) 240–800 keV, (P4) 800–2,500 keV, (P5) 2,500–6,900 keV, and (P6) >6,900 keV. In addition, the P6 channel also has a useful response to electrons with $E \gtrsim 700$ keV when the proton intensity is not too high (Yando et al., 2011). Access to the silicon detectors in each telescope is restricted by passive shielding with an entrance aperture that defines a 15° half-angle nominal FOV, within which each channel is typically assumed to have a uniform angular response. The proton telescope also includes a permanent magnet intended to deflect lower energy electrons away from the silicon detectors.

The true energy response of each channel to electrons and protons over a wide range of energies, accounting for atomic and nuclear interactions within the telescope structure, has been estimated by Monte Carlo simulation of particle trajectories through mechanical models of the electron and proton telescopes using the Geant4 software package (Yando et al., 2011). Simulated energy deposits from the silicon particle detectors in each telescope were binned, according to logic conditions that define each electron and proton channel, to compute corresponding energy response functions. Additional analysis of the same simulation results is used here to compute angular response functions, as described below, for both electrons and protons (though only the electron response is used in subsequent analysis).

Given a model radiation belt particle environment at a given satellite, the expected counting rate in MEPED channel i is

$$r_i = \int \int j(E, \alpha) A_i(E, \theta_t) dE d\Omega, \quad (1)$$

where j is particle intensity as a function of E and local pitch angle α ; A_i is the channel response function, or effective area, as a function of E and angle θ_t from the telescope axis; and Ω is solid angle. For an isotropic j , independent of α , this becomes

$$r_i = \int j(E) G_i(E) dE, \quad (2)$$

where the geometry factor, or energy response function, is

$$G_i = \int A_i(E, \theta_t) d\Omega. \quad (3)$$

The Geant4 simulation did not include enough electrons to compute accurate response functions at θ_t values well outside the nominal FOV, where detection efficiency is low. Therefore, they are approximated here by dividing the energy range for each channel into N intervals (two for protons and three for electrons) and assuming the response function A_{ik} for each interval k , from E_k to E_{k+1} , is separable as

$$A_{ik}(E, \theta_t) = G_i(E) a_{ik}(\theta_t), \quad (4)$$

where the angular response a_{ik} is normalized such that

$$\int a_{ik}(\theta_t) d\Omega = 1. \quad (5)$$

The rate r_i is computed using (4) in place of A_i in (1) and summing over the energy intervals:

$$r_i = \sum_{k=1}^N \int_0^{2\pi} \int_0^\pi \int_{E_k}^{E_{k+1}} j(E, \alpha(\theta_t, \phi_t)) G_i(E) dE a_{ik}(\theta_t) \sin \theta_t d\theta_t d\phi_t, \quad (6)$$

where local pitch angle α is a function of θ_t and azimuth ϕ_t about the telescope axis for a given telescope direction relative to the local magnetic field.

The Geant4 simulations included n_m incident electrons or protons at each selected energy E_m , with directions sampled randomly from an isotropic distribution inside a sphere of radius R . The geometry factor at energy m is obtained from Equation (2) by replacing j with the fluence $n_m \delta(E - E_m) / (4\pi^2 R^2)$ and r_i with the number of simulated counts n_{im} in channel i . Then

$$G_i(E_m) = 4\pi^2 R^2 \frac{n_{im}}{n_m}. \quad (7)$$

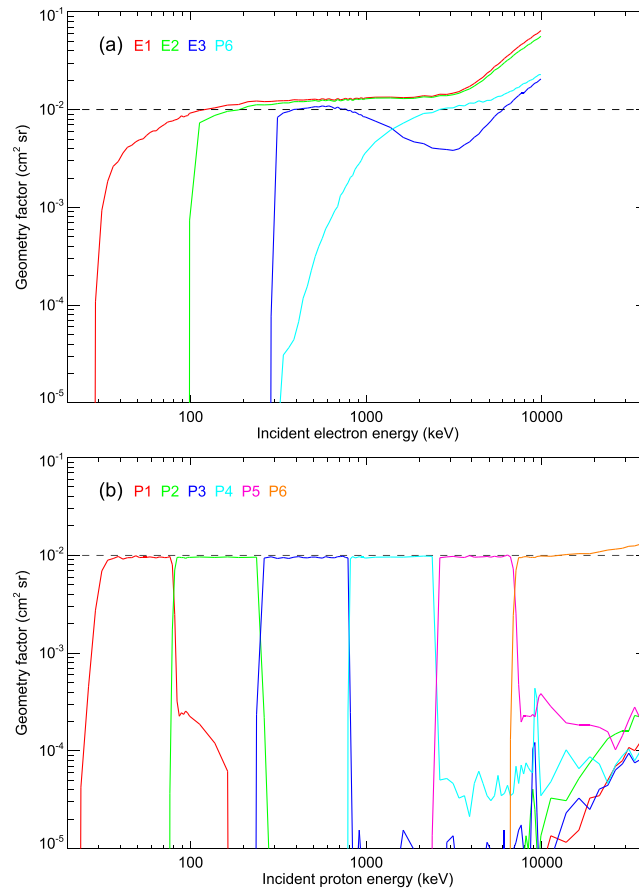


Figure 1. Geometry factors G_i , or energy response functions, color-coded for each of (a) the electron response of the three MEPED electron channels, E1, E2, and E3, and the P6 proton channel and (b) the proton response of the six proton channels, versus incident kinetic energy E , from Geant4 simulation results (Yando et al., 2011). The nominal $G = 0.01 \text{ cm}^2 \text{ sr}$ is also shown (dashed).

Geometry factors G_i for each channel i were computed by Yando et al. (2011) and are shown in Figure 1 for electrons and protons. They are seen to be in good agreement with nominal energy ranges of each channel, as expected.

For the angular response, n_m is distributed among bins of width $\Delta\theta_t = 1^\circ$ in incident angle θ_t , with n_{iml} the number simulated counts in channel i from bin l at $\theta_t = \theta_{il}$. Then, from Equation (6) for bin l with the same replacement for j and substituting (7),

$$a_{ik}(\theta_{il}) = \frac{1}{2\pi \sin \theta_{il} \Delta\theta_t} \frac{\sum_m n_{iml}}{\sum_m n_{im}}, \quad (8)$$

where the summations over m include all incident energies E_m in range k . From (8) it is easy to verify the normalization (5).

Angular response functions a_{ik} , computed from the same Geant4 simulations, are shown in Figure 2 for electrons and Figure 3 for protons. Energy intervals were selected for each channel to be consistent, as far as possible, with the assumption that angular response is independent of energy within each interval, thus minimizing possible error caused by the low number of particle counts at high incidence angles. The nominal FOV response is generally dominant as expected. For electron channels, response from higher angles varies only slightly between energy intervals, showing that results should be insensitive to the precise choice of interval boundaries. For proton channels, it is much lower in the only energy interval (red in Figure 3), where G is significant, as shown in Figure 1b. Therefore, response outside the nominal FOV can likely be neglected for protons, as expected based on their relatively low scattering rates.

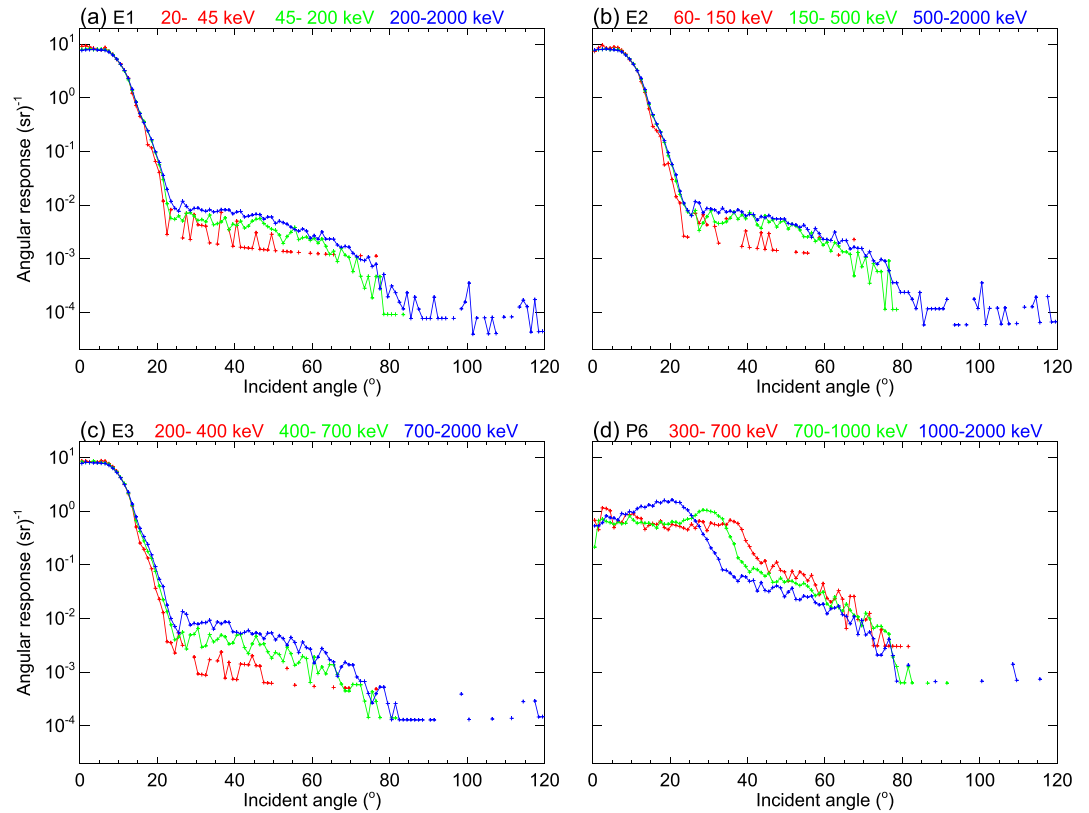


Figure 2. Angular response functions, a_{ik} , for each of four MEPED electron channels and three corresponding color-coded energy intervals, versus incident angle θ_i relative to the telescope axis, from Geant4 simulation.

We have assumed azimuthal symmetry in the angular response functions, corresponding to the mechanical configuration of each telescope, but the proton telescope's magnetic field causes some asymmetry in the electron response of channel P6 that is averaged over in computing the response function. The field also accounts for the off-center peak electron response (Figure 1d herein and Figure 7 of Yando et al., 2011).

3. Response to Model Electron Distributions

Computation of expected counting rates by equation (6), based on electron intensity and channel response functions, for comparison to measurements, requires a model of the electron distribution in E and α . The angular response to varying electron pitch angle distributions will be demonstrated with a simplified dynamical model for the radiation belt electron phase space density, $f = j/p^2$, near the loss cone:

$$\frac{\partial f}{\partial t} = \frac{1}{x} \frac{\partial}{\partial x} \left(x D_{xx} \frac{\partial f}{\partial x} \right) - \frac{4}{\tau_b} (1 - F_b) \Theta(x_c - x) f, \quad (9)$$

where p is momentum; t is time; $x = \cos \alpha_0$; α_0 is equatorial pitch angle; τ_b is bounce period evaluated at x_c , the x value of the equatorial loss cone angle α_{0c} ; the x dependence of τ_b is neglected; F_b is a fraction of electrons that backscatter from the atmosphere; Θ is a unit step function specifying that electrons are lost only inside the loss cone; and the diffusion coefficient

$$D_{xx} = y^2 D_w + y^2 D_b \Theta(x_c - x) \quad (10)$$

with $y = \sin \alpha_0$ includes a plasma wave contribution D_w at all x and a backscatter contribution D_b inside the loss cone. The backscatter diffusion coefficient D_b approximates changes in pitch angle that occur during the backscatter process (Selesnick et al., 2004). The y^2 factors are included so that the diffusion coefficient in α_0 , $D_{\alpha_0 \alpha_0} = D_{xx}/y^2$, is independent of α_0 as expected to be approximately true near α_{0c} (Albert et al., 2020). Boundary conditions for (9) are $\partial f/\partial x = 0$ at $x = 0$ and $x = 1$.

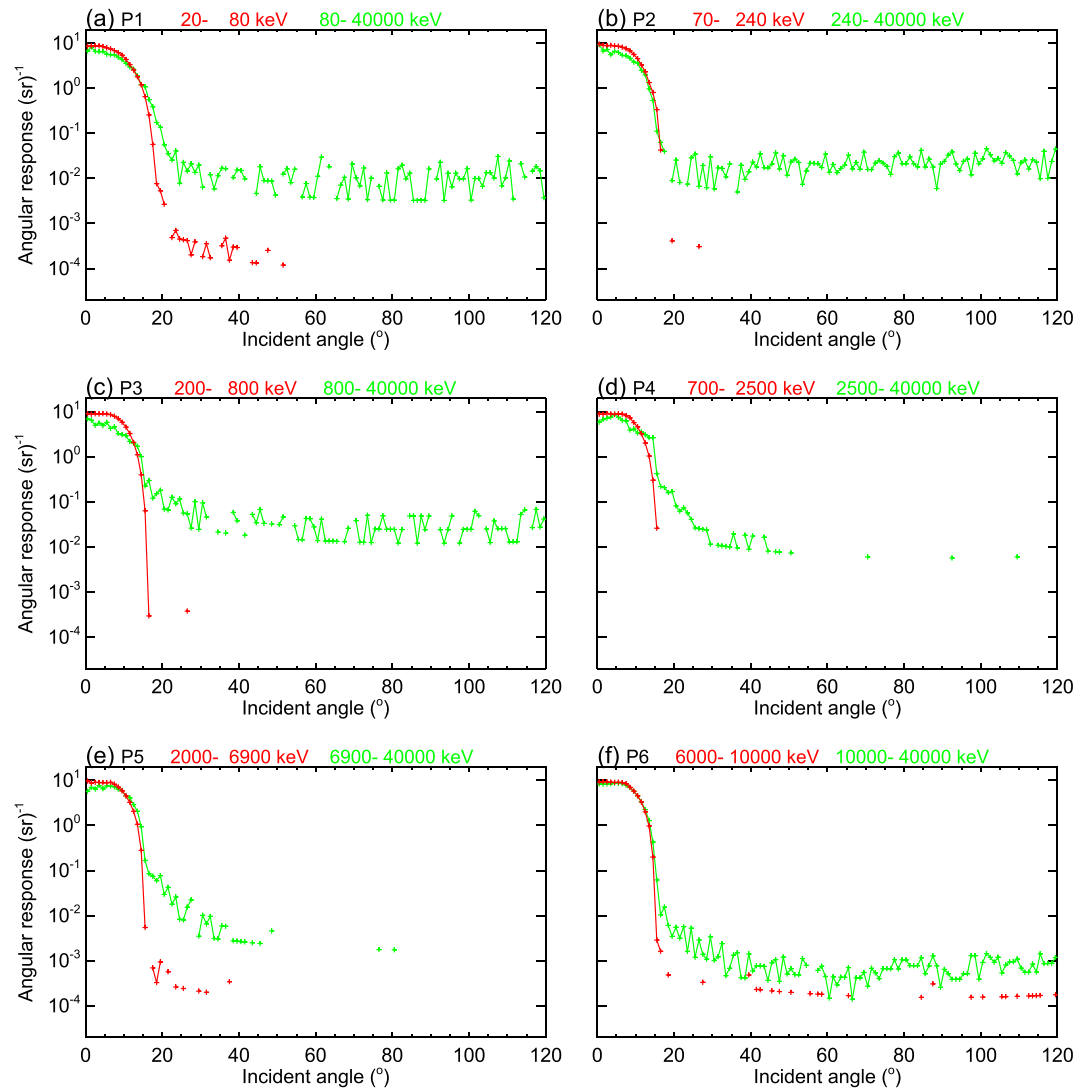


Figure 3. Similar to Figure 2 but for protons in each of six MEPED channels with two corresponding color-coded energy intervals.

The model Equation (9) is solved numerically for f by finite differencing, using the semi-implicit Crank-Nicholson method for the diffusion term (Press et al., 1992), and integrating until a steady pitch angle distribution is reached, independent of the initial condition, that only decays in time. Sample results are shown in Figures 4a and 4b, after converting from f to j and from x to local pitch angle α , at a typical POES or MetOp satellite location, and weighting by an exponential energy spectrum, $j \sim e^{-E/E_0}$ with $E_0 = 300$ keV. Diffusion coefficients are $D_w = 10^{-2}$ and 10^{-6} s $^{-1}$, with $D_b = 10^{-5}$ s $^{-1}$ in each case.

Rates in each channel are then evaluated using (6), with typical telescope axis pitch angles of 10° for the 0° telescope and 80° for the 90° telescope (the vertical direction of the 0° telescope is never aligned exactly with the local magnetic field). To determine the ranges of pitch angles to which each rate responds for a given electron intensity model, distributions in α are computed by replacing j in (6) with weighted δ functions at each α and are shown in Figures 4c and 4d. Integration of these distributions over α gives the total counting rate for each channel, as computed directly from (6). They show that, for the 90° telescope, the response is almost entirely from pitch angles within the nominal $\pm 15^\circ$ telescope FOV, as expected. The same is true for the 0° telescope when D_w is high (Figure 4c). However, when D_w is low (Figure 4d), the response is from pitch angles similar to that of the 90° telescope, because there are insufficient electrons in the loss cone at low α to produce any significant response from pitch angles in the nominal FOV.

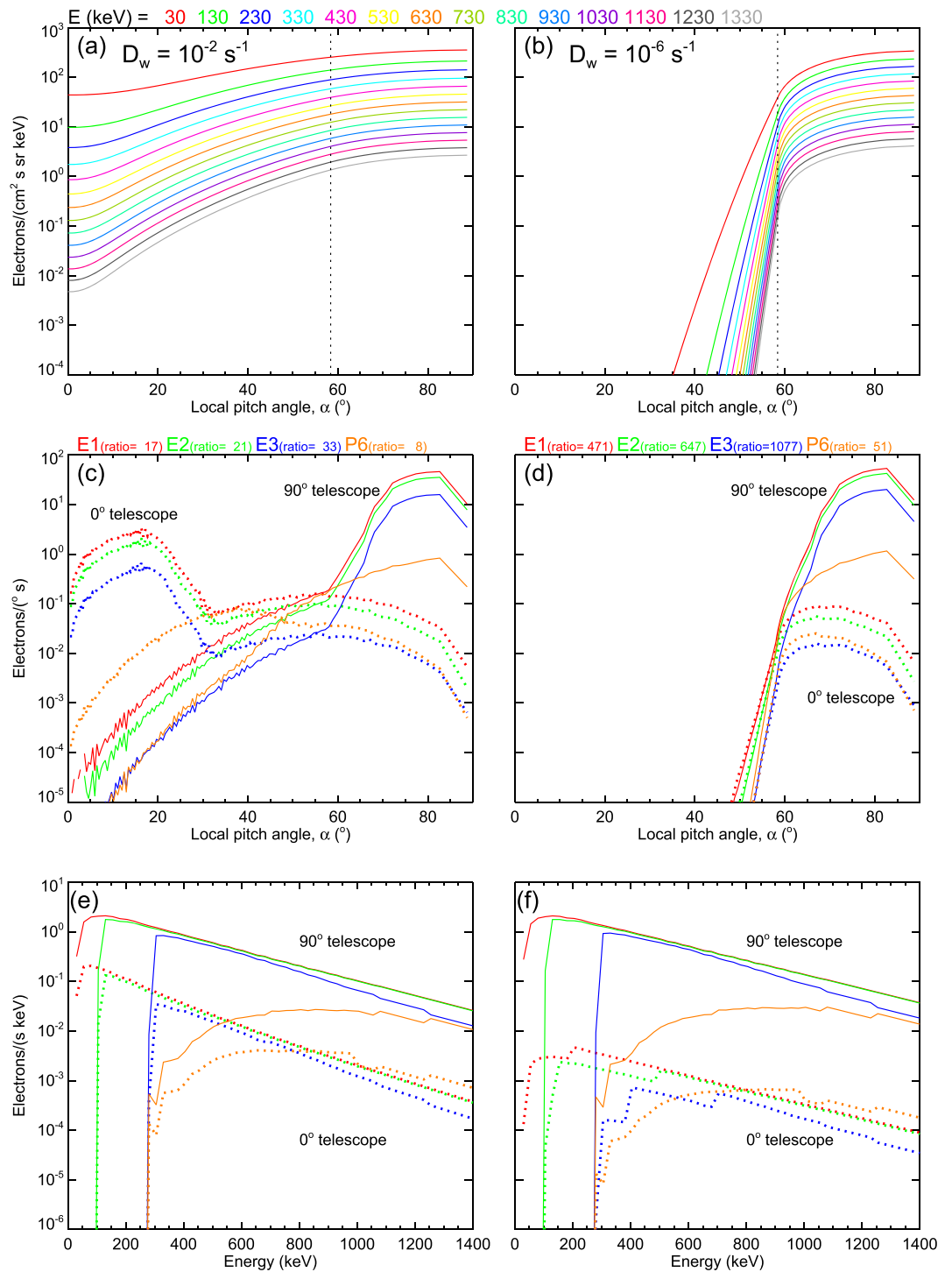


Figure 4. Model electron local pitch-angle distributions color-coded by energy (top row), and corresponding counting rate distributions in pitch angle (middle row) and energy (bottom row) color coded by MEPED channel. High-diffusion (left column) and low-diffusion (right column) cases are included. Counting rate distributions are shown for the 0° (dotted) and 90° (solid) telescopes. Ratios of 90° to 0° total counting rates are listed for each channel (above the middle row). Loss cone angles are indicated (dotted, top row).

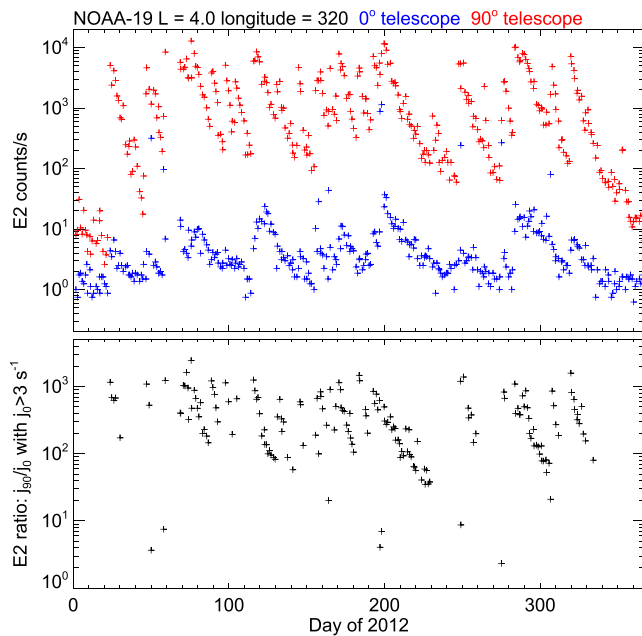


Figure 5. (a) Counting rate data from channel E2 of the NOAA-19 satellite 0° (blue) and 90° (red) telescopes versus day of year in 2012. Data are from the closest location to $L = 4$ and 320° longitude during each day. (b) Ratios of the 90° to 0° rates when both rates are higher than 3 counts/s.

Ratios of 90° to 0° total counting rates, derived from (6), are listed above Figures 4c and 4d. For example, the channel E3 ratio is 33 in the high-diffusion case and 1,077 in the low-diffusion case. The high-diffusion ratio is a true reflection of trapped electron intensity relative to loss cone intensity, but this is not the case for the low-diffusion ratio because the true loss-cone intensity is too low to be observed. If an idealized angular response were used instead, with uniform response inside the FOV and no response outside, ratios with high D_w would be similar for channels E1, E2, and E3, though somewhat higher for P6, but with low D_w all ratios would be many orders of magnitude higher than those computed with the more accurate angular response functions. A value of $D_w \sim 10^{-3}$ would be required with the idealized angular response to obtain ratios, for the electron telescope channels, similar to those obtained with $D_w = 10^{-6}$ (Figure 4d) using the more accurate angular response. Thus, the idealized response would cause a factor $\sim 10^3$ overestimate of D_w in this low-diffusion case.

Distributions in energy, computed similarly to the distributions in α , are shown in Figures 4e and 4f. Integrated over energy, they would also give total counting rates as computed directly from (6). They are broad because of the integral nature of the channel response functions. For the low-diffusion case, the 0° telescope distributions are weighted more toward higher energy, corresponding to a similar weighting within each response function outside the nominal FOV, except, again, for the P6 channel (see Figure 2).

4. MEPED Electron Data

Counting rate data as a function of time for the year 2012, from the E2 channel of each electron telescope, measured by the NOAA-19 satellite (launched 6 February 2009) at $L = 4$ and 320° longitude in the southern hemisphere, are shown in Figure 5a. The geographic location was chosen so that the 90° telescope data represent stably trapped electron intensity, which is seen to vary considerably throughout the year. The 0° data show less variability, but this is, at least in part, due to a background that prevents the total rate from falling much below ~ 1 count/s. The ratio of rates from the two telescopes is shown in Figure 5b, including only times when both rates were well above background. The ratio also shows significant variability that spans the range shown in Figure 4, ~ 30 –1,000, as representative of high to low diffusion. Times when the ratio is near or below the low end of this range are candidates for days in which the 0° data represent true loss cone electrons. However, because the ratio varies continuously, there is no clear demarcation of such data, and a closer inspection is required.

Observed rates at $L = 4$ from all four electron channels on six operational satellites are shown as a function of magnetic longitude in Figures 6, 7, and 8 for data taken in 2012 during 6-hr intervals on 13, 15, and 16 October, respectively (days of year 287, 289, and 290 for reference to Figure 5). These days were chosen as representing differing conditions during an interval when the stably trapped intensity is relatively high following an electron injection event. Figures 7 and 8 also include model simulations of the data that will be described in the next section. Also shown below the data in all three figures are the equatorial and local pitch angles of the telescope axes, with ranges representing the nominal $\pm 15^\circ$ FOVs, the northern and southern 100-km altitude equatorial bounce loss cone (BLC) angles, and the corresponding drift loss cone (DLC) angle. These are computed with the IGRF-12 magnetic field model (Thébault et al., 2015) and no external field model.

It is apparent that the longitude distributions of the rate data are disordered in Figure 6 but are well ordered in Figures 7 and 8, where they vary in close coordination with changes in telescope pitch angle relative to the BLC and DLC angles. The disordered case often includes low 90° to 0° ratios, suggesting high pitch-angle diffusion but with significant time variation. The ordered distributions have generally high ratios, suggesting low pitch-angle diffusion and little or no time dependence during the 6-hr intervals represented. In each of the ordered cases, rates observed near 0° and 360° longitude in the Northern Hemisphere by the 90°

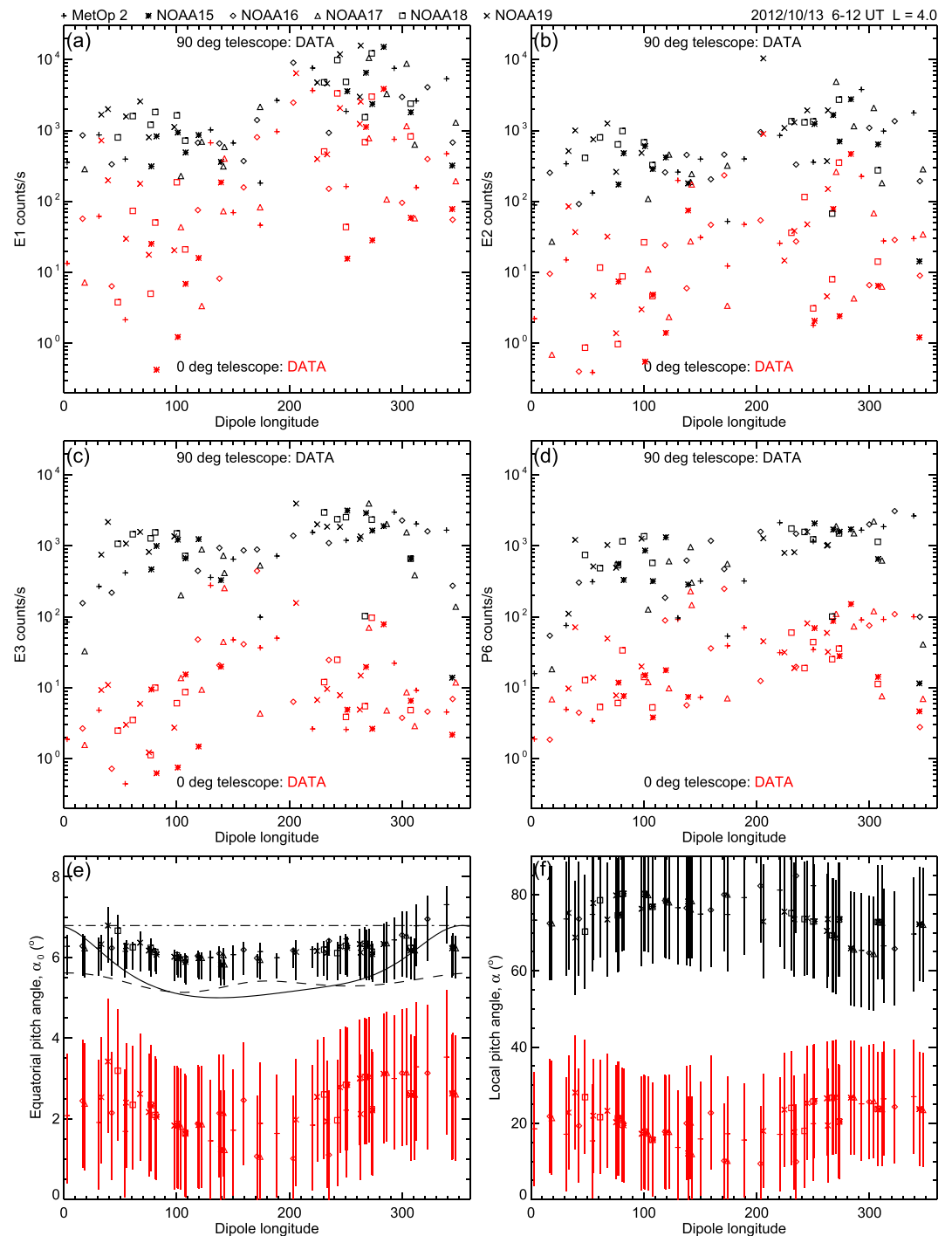


Figure 6. (a–d) Counting rate data from each of the four electron channels on six operational satellites, coded by symbol type, taken at $L = 4$ from 6 to 12 hr UT on 13 October 2012, versus dipole longitude. Data from the 0° (red) and 90° (black) telescopes are included. (e) Corresponding equatorial pitch angles of the telescope axes for each data point, with the range covered by the nominal $\pm 15^\circ$ FOV. North (dashed) and south (solid) BLC angles and the DLC angle (dash-dot) are indicated. (f) Corresponding local pitch angles of the telescope axes for each data point with FOV ranges.

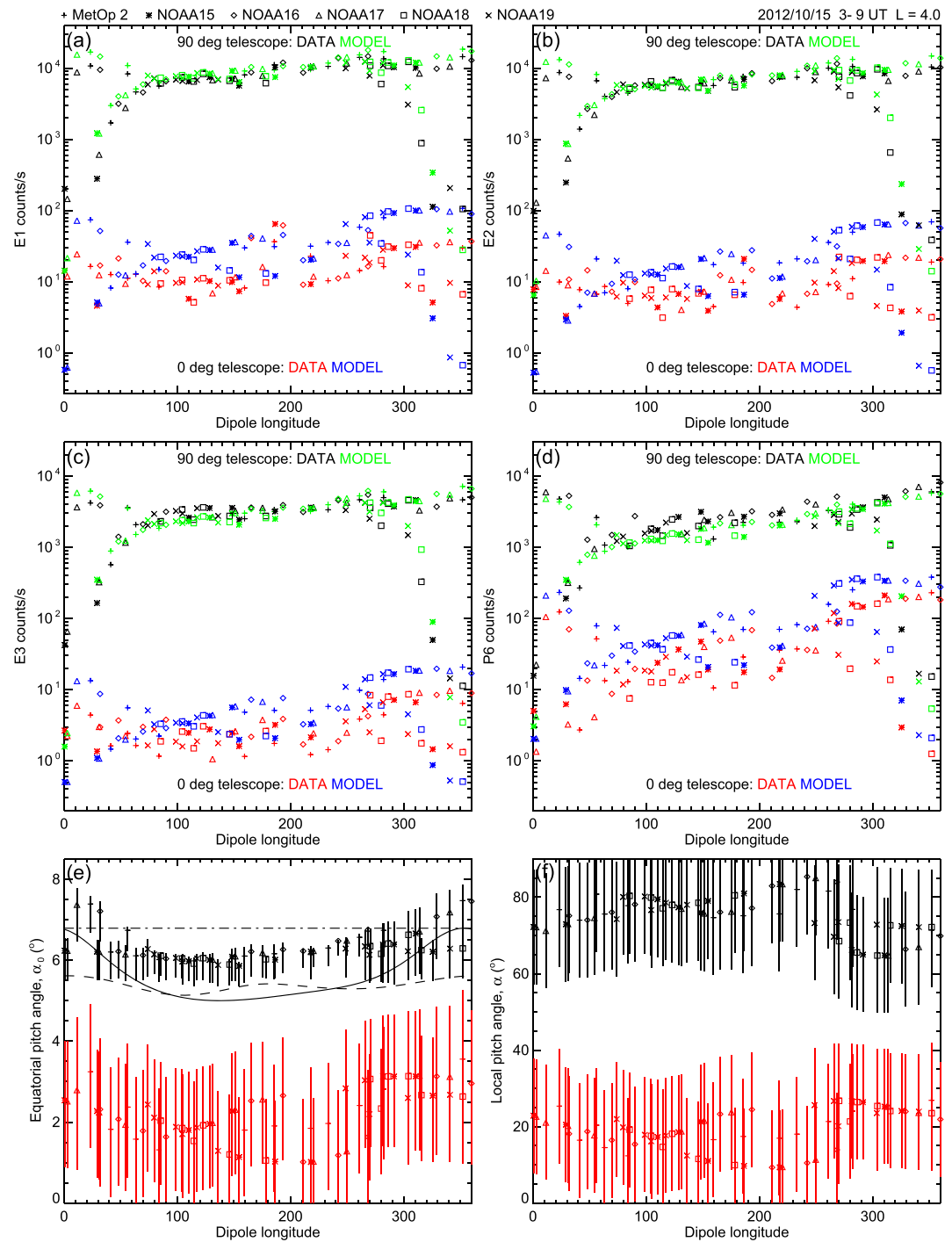


Figure 7. Similar to Figure 6 but for data taken from 3 to 9 hr UT on 15 October 2012. Model simulations of each data point are also included for the 0° (blue) and 90° (green) telescopes.

telescope are generally lower than those observed at the same longitudes in the Southern Hemisphere by the 0° telescope, despite the entire nominal FOV of the 0° telescope being at lower pitch angle than that of the 90° telescope. This again strongly suggests that the 0° telescope is in fact responding to electrons outside its nominal FOV, and outside the BLC; otherwise, the loss cone electron distribution would have to increase toward lower pitch angles.

Sample data have been selected at $L = 4$ because electron intensity there is high and proton contamination is unlikely. Similar results can be obtained at other L values so long as the orientation of each telescope relative

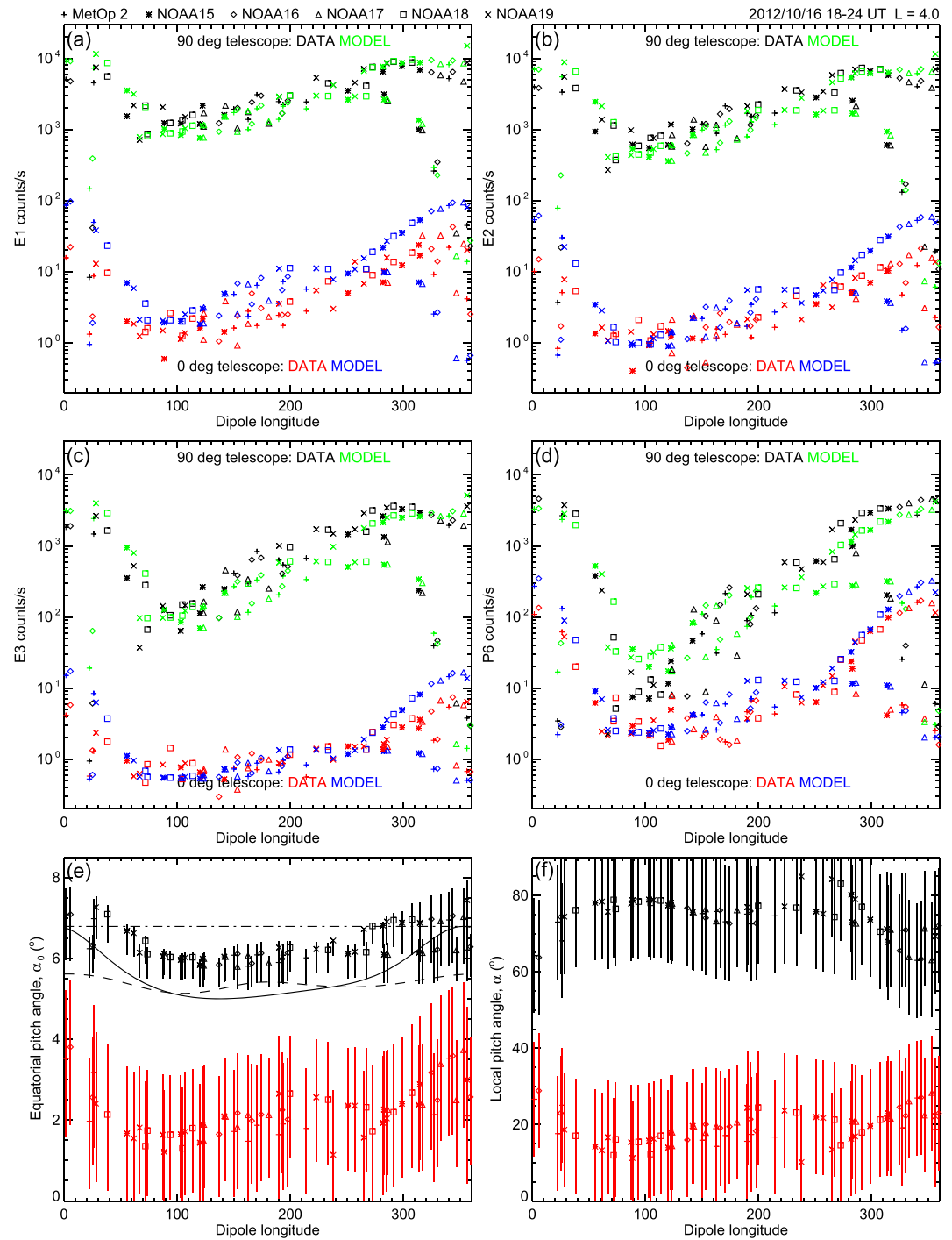


Figure 8. Similar to Figure 7 but for data taken from 18 to 24 hr UT on 16 October 2012.

to the local magnetic field is fully accounted for. (Roles are reversed at the lowest L values, with the vertical 0° telescope closer to field aligned.)

5. Simulation of MEPED Electron Data

The data discussed in the previous section allowed some inferences to be made concerning the observed electron distributions but, because of ambiguity caused by broad angular response functions, a quantitative assessment requires comparison to model predictions. For the disordered case of Figure 6 the diffusion

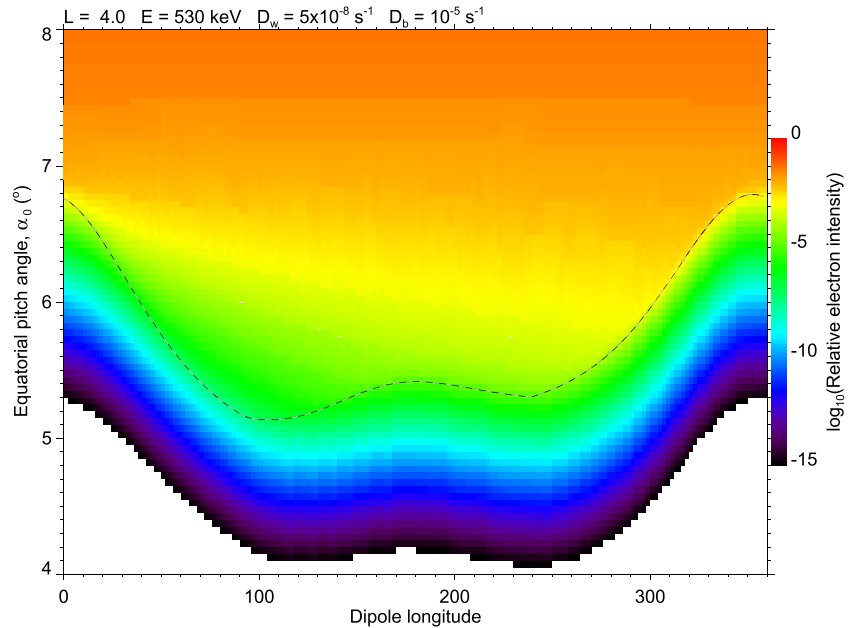


Figure 9. Model color-coded electron intensity as a function of equatorial pitch angle and dipole longitude, with selected values of energy and the diffusion coefficients at $L=4$. The BLC angle is indicated (dashed).

model calculations of section 3 could be used to fit each pair of data points in a similar way to the previous work based on ratios of 90° and 0° telescope data (Li et al., 2013), but using the full response functions. That is not attempted here, but we can expect that, where diffusion is high enough, results would be similar.

For the ordered cases of Figures 7 and 8, we modify the model to account for longitudinal variation by including azimuthal drift:

$$\frac{\partial f}{\partial t} + \omega_d \frac{\partial f}{\partial \phi} = \frac{1}{x} \frac{\partial}{\partial x} \left(x D_{xx} \frac{\partial f}{\partial x} \right) - \frac{4}{\tau_b} (1 - F_b) \Theta(x_c - x) f, \quad (11)$$

where ω_d is drift frequency, approximated by the value in a dipole magnetic field at $x = x_c$, and ϕ is drift phase or magnetic (dipole) longitude. In the model f is independent of bounce phase, and the equatorial BLC angle at each longitude is the maximum of the northern and southern values, computed from the IGRF as before (Figures 6 to 8). Boundary conditions are $\frac{\partial f}{\partial x} = 0$ at $x=0$ and 1, as before, and $f(\phi, x, t) = f(\phi + 2\pi, x, t)$.

Numerical solution of the model Equation (11) now employs operator splitting with Crank-Nicholson differencing in the x direction and upwind differencing in the ϕ direction (Press et al., 1992). An initial condition for f is assumed, which then evolves over the course of a single drift period at each energy. This is sufficient for comparison to POES data because the low-altitude part of the electron distribution quickly reaches an equilibrium, independent of the initial condition, that subsequently only decays in time. A sample solution shown as a function of α_0 and ϕ in Figure 9 illustrates filling of the DLC by pitch-angle diffusion, as electrons drift eastward toward the South Atlantic Anomaly (SAA, ~ 300 to 30° longitude), and lower intensity in the BLC.

Solutions are computed at energies from 30 to 1,405 keV, spaced by 25 keV, and weighted by the assumed exponential energy spectra. Then rates are simulated for each channel by evaluating Equation (6), using the telescope pitch angles for each data point and the satellite model magnetic field for converting equatorial to local pitch angle. Finally, constant background rates, estimated for each channel from the lowest levels reached by the 0° telescope data, are added to each simulated data point.

Simulated rates have been fit to the 90° telescope data of Figures 7 and 8 by adjusting D_w , D_b , E_0 , and an overall scaling factor. Wave diffusion coefficients obtained from the fit, and used for the simulated data shown, are $D_w = 10^{-6} \text{ s}^{-1}$ for Figure 7 and $D_w = 5 \times 10^{-8} \text{ s}^{-1}$ for Figure 8; $D_b = 10^{-5} \text{ s}^{-1}$ and $E_0 = 300 \text{ keV}$ are common to both figures.

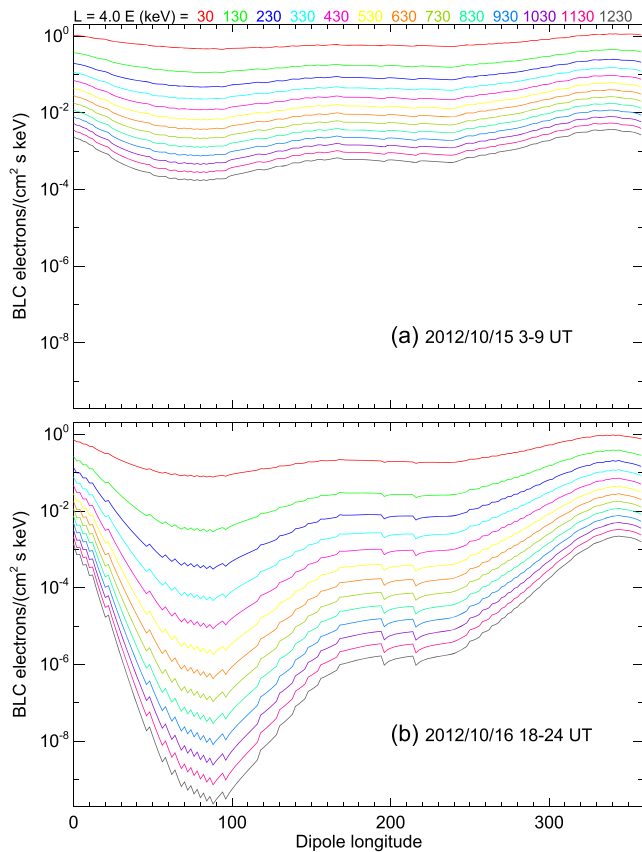


Figure 10. Model omnidirectional electron intensity in the BLC or, apart from backscattering, precipitating electron flux, versus dipole longitude and color coded by energy, at $L = 4$ for the high- and low-diffusion coefficients of (a) Figure 7 and (b) Figure 8, respectively.

and longitude in Figure 10 for each of the two cases discussed above (Figures 7 and 8). This represents precipitating electron flux into the atmosphere, except that no reduction has been applied to account for backscattering, assumed in the model to be 20%. It is seen that maximum precipitating fluxes in the SAA region, near longitude 350° , are similar but that precipitation is significantly reduced at other longitudes for the lower diffusion case due to the relatively empty DLC.

7. Discussion

Angular response functions show that the MEPED telescopes have relatively low sensitivity to electrons well outside their nominal $\pm 15^\circ$ FOV (Figure 2). However, for the 0° telescope, electron intensity there is usually much higher, and the sensitivity is sufficient that data are usually dominated by electrons from those high incidence angles, in a similar range of pitch angles to electrons measured by the 90° telescope. Therefore, the 0° telescope usually measures stably trapped or quasi-trapped (drift loss cone) electrons, rather than precipitating (bounce loss cone) electrons as would be expected based on its orientation. (Exceptions occur when pitch angle diffusion is sufficiently enhanced, or when even the 90° telescope measures precipitating electrons.)

This conclusion is suggested by the usually high observed counting rate ratios between the 90° and 0° telescopes (Figure 5). It is confirmed by verifying that, most of the time, longitude distributions are ordered (similar to Figure 7 or 8) rather than disordered (Figure 6). Whether the 0° telescope is responding to precipitating electrons at any given time can only be established, in a model dependent way, by data simulation for each channel accounting for the full instrumental response function, including angular response (Figure 4).

When the full response is included, computed precipitating electron flux is typically much lower than would be expected on the basis of 90° to 0° flux ratios, except when diffusion rates are high. The model omni-

These D_w values are, respectively, at and below the low-diffusion case of Figure 4, confirming that the 0° telescope data represent trapped or quasi-trapped (DLC) electrons in each case, rather than precipitating electrons as would be expected from their near alignment to the local magnetic field. The lower D_w required for Figure 8 relative to Figure 7 results from the relatively empty DLC, as shown by lower counting rates near longitude 100° . The 0° data were not included in the fit because of uncertainty in angular response functions outside the nominal FOV. They are seen to be consistently somewhat lower than predicted by the model in each case but are otherwise in reasonable agreement.

We note that it would be impossible to obtain a reasonable fit to all of the data in Figure 7 or 8 using an idealized, FOV-only angular response. If the same model diffusion coefficients were used, then simulated 0° data would be too low by many orders of magnitude. They could be near observed values if D_w were increased by several orders of magnitude (depending on energy), but then the DLC would be filled and the observed longitude dependence would not be achieved.

6. Precipitating Electron Flux

When a satellite is in the Northern Hemisphere and conjugate to the SAA region, it measures electrons entirely within the BLC, even with the 90° telescope. When diffusion is low enough that the 0° telescope otherwise responds only to trapped or DLC electrons, these 90° data provide the strongest constraint on BLC intensity. They are shown in Figures 7 and 8 as low counting rates near longitude 0° and 360° , which are near or below corresponding 0° telescope data from the Southern Hemisphere as mentioned in section 4. The backscatter diffusion value of $D_b = 10^{-5} \text{ s}^{-1}$ was adjusted to approximately match these data with the model simulations.

Model omnidirectional intensity in the BLC, computed by integrating model intensity over solid angle for $x > x_c$, is shown as a function of energy

directional BLC flux (Figure 10) includes all electrons mirroring below 100 km, but many of these would not reach lower altitude. The precipitating flux at 50 km, for example, would be even lower but could be computed in a similar way.

Accuracy of computed precipitation flux depends on the fidelity of the model simulation. In our case a simplified dynamical model neglected several factors that could be significant. For example, it assumed that electron intensity is independent of bounce phase with a single loss cone angle at each longitude, that atmospheric backscatter can be approximated as a diffusion process, that diffusion coefficients are independent of local time, and that the external magnetic field can be neglected. Improved modeling that properly accounts for these and other factors, either theoretically (Selesnick et al., 2004) or empirically, might lead to better fits to the data and more accurate results.

It is clear from the model fits to sample data (Figures 7 and 8) that simulated counting rates of the 0° telescope is consistently overestimated, by factors ~2. This could result from error in the model stably trapped or quasi-trapped electron pitch angle distributions, just outside the local bounce loss cone, because, although the two telescopes respond to the same range of electron pitch angles, they do so with different weighting (Figure 4d). A need for improved modeling is again indicated.

Inaccuracy can also result from error in the response functions at incidence angles well outside the nominal FOV where they have not been well determined by Geant4 simulation. Further error is likely if some of these high-incidence angles are partially blocked by the satellite body or by other instrumentation, a factor that, if included in the Geant4 simulation, would reduce computed response at those angles. However, it is already apparent that the available response functions provide significant improvement, relative to a nominal FOV response, in the reliability of MEPED electron data interpretation.

Data Availability Statement

POES and MetOp SEM-2 data are available online (from <https://ngdc.noaa.gov/stp/satellite/poes>). MEPED electron and proton response functions derived in this work are included in supplementary information and are also available online (from <https://doi.org/10.5281/zenodo.3985955>).

Acknowledgments

This work was supported by the Space Vehicles Directorate of the Air Force Research Laboratory. Contributions by W. Tu were partially supported by NSF Grant AGS 1752736 and NASA Grant 80NSSC18K1284.

References

- Albert, J. M., Starks, M. J., Selesnick, R. S., Ling, A. G., O'Malley, S., & Quinn, R. A. (2020). VLF transmitters and lightning-generated whistlers: 2. Diffusion of radiation belt electrons. *Journal of Geophysical Research: Space Physics*, *125*, e2019JA027030. <https://doi.org/10.1029/2019JA027030>
- Evans, D. S., & Greer, M. S. (2000). Polar Orbiting Environmental Satellite Space Environmental Monitor—2: Instrument descriptions and archive data documentation: Natl. Atmos. and Oceanic Admin., Space Environ. Cent., Boulder, Colo.
- Li, W., Ni, B., Thorne, R. M., Bortnik, J., Green, J. C., Kletzing, C. A., et al. (2013). Constructing the global distribution of chorus wave intensity using measurements of electrons by the POES satellites and waves by the Van Allen Probes. *Geophysical Research Letters*, *40*, 4526–4532. <https://doi.org/10.1002/grl.50920>
- Nesse Tysøy, H., Sandanger, M. I., Ødegaard, L. K. G., Stadsnes, J., Aasnes, A., & Zawedde, A. E. (2016). Energetic electron precipitation into the middle atmosphere—Constructing the loss cone fluxes from MEPED POES. *Journal of Geophysical Research: Space Physics*, *121*, 5693–5707. <https://doi.org/10.1002/2016JA022752>
- Ni, B., Li, W., Thorne, R. M., Bortnik, J., Green, J. C., Kletzing, C. A., et al. (2014). A novel technique to construct the global distribution of whistler mode chorus wave intensity using low-altitude POES electron data. *Journal of Geophysical Research: Space Physics*, *119*, 5685–5699. <https://doi.org/10.1002/2014JA019935>
- Peck, E. D., Randall, C. E., Green, J. C., Rodriguez, J. V., & Rodger, C. J. (2015). POES MEPED differential flux retrievals and electron channel contamination correction. *Journal of Geophysical Research: Space Physics*, *120*, 4596–4612. <https://doi.org/10.1002/2014JA020817>
- Pettit, J. M., Randall, C. E., Peck, E. D., Marsh, D. R., van de Kamp, M., Fang, X., et al. (2019). Atmospheric effects of >30-keV energetic electron precipitation in the Southern Hemisphere winter during 2003. *Journal of Geophysical Research: Space Physics*, *124*, 8138–8153. <https://doi.org/10.1029/2019JA026868>
- Pham, K. H., Tu, W., & Xiang, Z. (2017). Quantifying the precipitation loss of radiation belt electrons during a rapid dropout event. *Journal of Geophysical Research: Space Physics*, *122*, 10,287–10,303. <https://doi.org/10.1002/2017JA024519>
- Press, W. H., Teukolsky, S. A., Vetterling, W. T., & Flannery, B. P. (1992). *Numerical recipes in C: The art of scientific computing*, 2nd ed. Cambridge: Cambridge University Press.
- Rodger, C. J., Clilverd, M. A., Green, J. C., & Lam, M. M. (2010). Use of POES SEM-2 observations to examine radiation belt dynamics and energetic electron precipitation into the atmosphere. *Journal of Geophysical Research*, *115*, A04202. <https://doi.org/10.1029/2008JA014023>
- Selesnick, R. S., Looper, M. D., & Albert, J. M. (2004). Low-altitude distribution of radiation belt electrons. *Journal of Geophysical Research*, *109*, A11209. <https://doi.org/10.1029/2004JA010611>
- Soria-Santacruz, M., Li, W., Thorne, R. M., Ma, Q., Bortnik, J., Ni, B., et al. (2015). Analysis of plasmaspheric hiss wave amplitudes inferred from low-altitude POES electron data: Validation with conjunctive Van Allen Probes observations. *Journal of Geophysical Research: Space Physics*, *120*, 8681–8691. <https://doi.org/10.1002/2015JA021148>

- Thébault, E., Finlay, C. C., Beggan, C. D., Alken, P., Aubert, J., Barrois, O., et al. (2015). International Geomagnetic Reference Field: the 12th generation. *Earth, Planets, and Space*, *67*, 79. <https://doi.org/10.1186/s40623-015-0228-9>
- Yando, K., Millan, R. M., Green, J. C., & Evans, D. S. (2011). A Monte Carlo simulation of the NOAA POES Medium Energy Proton and Electron Detector instrument. *Journal of Geophysical Research*, *116*, A10231. <https://doi.org/10.1029/2011JA016671>